PHYSICAL REVIEW FLUIDS **6**, 113701 (2021)

Nonsymmetric ionic transport in a nonbinary electrolyte at high voltage

Arnon Ratzabi,[1] Tal Eluk,[2] Avi Levy,[1] and Yuri Feldman[1,*]
[1]*Department of Mechanical Engineering, Ben-Gurion University of the Negev,*
P.O. Box 653, Beer-Sheva 84105, Israel
[2]*Hewlett Packard Indigo Division, P.O. Box 150, Rehovot 76101, Israel*

(Received 11 January 2021; accepted 25 October 2021; published 19 November 2021)

Ionic transport in one- and two-dimensional (2D) electrolytic cells operating at high voltage with a nonsymmetric electrolyte consisting of three species is simulated numerically. The numerical simulations are aimed at elucidating the differences in the onset of the electroconvective instability in the nonsymmetric electrolyte in a 2D electrolytic cell compared with that for a symmetric binary electrolyte. An extensive parametric study is performed to determine the mechanisms governing the onset of the instability. In addition, the main characteristics of the spatiotemporal evolution of the electroconvective instability are investigated. By focusing on the characteristics typical of the onset of the electroconvective instability in a nonsymmetric electrolyte, we are able to offer a physical interpretation and a detailed discussion of the origin and development of this instability.

DOI: 10.1103/PhysRevFluids.6.113701

I. INTRODUCTION

Electroconvection (EC) in a fluid resulting from an externally applied electric field driving counterions toward an ion-selective surface plays a significant role in various engineering applications, including energy harvesting by reverse electrodialysis [1–6], electrochemical deposition of ramified growths (including control of dendrite growth in batteries [7,8]), fabrication of microchips [9], operation of micro- and nanofluidic devices (such as micropumps operating in fuel cells [10,11], preconcentrators [12], micromixers [13], semiconductors [14,15], biosensors [16,17], and fluidic diodes [3,18–23]), electrochemical machining [24], and acid-recovery technologies in metallurgy [25–27], to name but a few.

When characterizing ionic transport within an electrolyte confined by a single surface or by a pair of ion-selective surfaces and subjected to an externally applied voltage, it is common to focus on the shape of the current-voltage curve. This curve has three distinguishable regimes: an Ohmic regime, observed at low voltages and characterized by a constant positive slope; a limiting regime, in which the concentration polarization (CP) phenomenon results in a diffusion limitation associated with a depleted extended space-charge (ESC) layer and a saturated current [28,29]; and an overlimiting regime, typical of the highest voltages and characterized by a re-increasing slope [30]. The overlimiting regime has commanded most of the attention over the past two decades because it constitutes a critical factor in the fundamental understanding of convective ionic transport within an electrolyte and because it is a common phenomenon in many engineering applications.

The presently existing consensus that relates the overlimiting regime to the electroconvective instability (ECI) resulting from a tangential electric field acting upon the ESC associated with a nonequilibrium electric double layer (EDL) may be attributed to the seminal theoretical work of Ref. [30]. This work was subsequently extended by further theoretical developments [31–33] and confirmed by experimental results [34,35]. Together, these studies have motivated further research

---

[*] yurifeld@bgu.ac.il

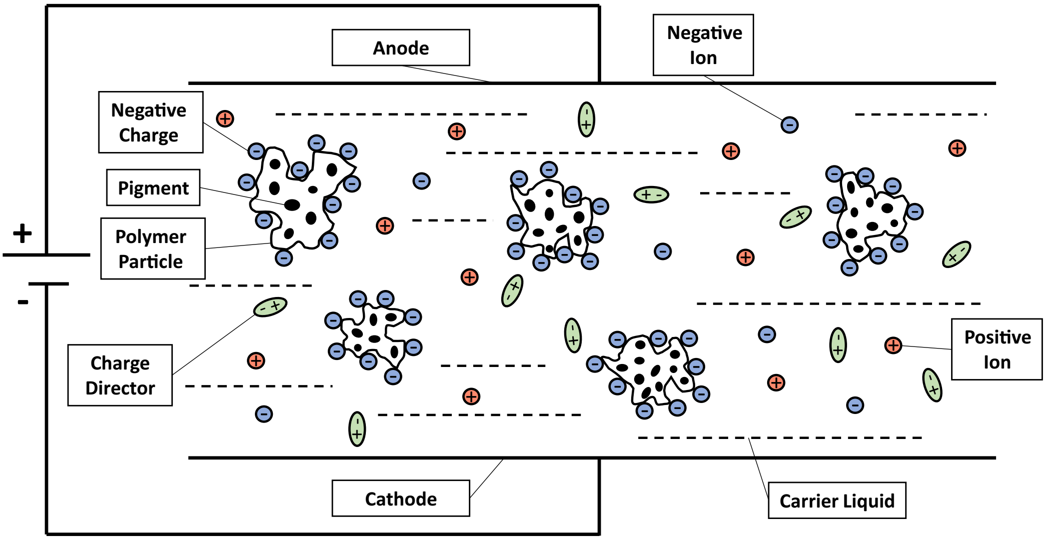

FIG. 1. Composition of the printer ink. Reprinted with permission of IS&T: The Society for Imaging Science and Technology sole copyright owners of The Journal of Imaging Science and Technology [40].

on the EC characteristics typical of the overlimiting regime. Among the numerous works on this topic, worth mentioning are an investigation of the potential of utilizing EC for the enhancement of mixing in a system with nonplanar periodic distortion of the cathode surface [36], the development of a unified theory of EC based on asymptotic and linear stability analysis [37], a recent investigation of the equilibrium ECI near a perfectly charged selective solid of finite conductivity [38], and a recent study on the impact of Joule heating on electroconvective ionic transport [39].

Against the above background, the motivation for the current study derives from a need to understand the physics governing two-dimensional (2D) convective flow, in general, and development of ECI, in particular, in the ink used in modern electrophotographic printers. The ink used in such HP printers, known as ElectroInk, comprises a nonsymmetric electrolyte containing a mixture of three species, namely, polymeric ink-containing particles and positively and negatively charged ions dissociated from charge director micelles under the action of a strong electric field. The ink carrier comprises an oily nonpolar electrically neutral liquid, namely IsoparTM-L [40], as shown in Fig. 1. In this context, the current study aims at addressing two major questions. First, to what extent does the ionic transport within the considered nonsymmetric electrolyte differ from that of its symmetric binary counterpart prior to development of ECI? And second, what are the physical mechanisms distinguishing the ECI onset scenario observed in the considered nonsymmetric electrolyte from that typical of a symmetric binary electrolyte?

The electrophotographic printer is a sophisticated machine whose operation relies on a series of sequential technological processes. Therefore, when seeking an improvement of printing quality, it is critical to first identify the node with the greatest operational uncertainty and then to focus on analyzing the electro-osmotic flow regime typical of this node. We argue that such a node is the gap between the main electrode (ME) and the developer roller (DR) (see Fig. 2), where the ECI development takes place, and in the framework of the current study we therefore focus on the analysis of the electroconvective ink flow within this gap.

We now briefly introduce the major characteristics of the electro-osmotic flow typical of the above configuration. As can be seen from Fig. 2, diluted ink enters the neck between the ME and the back electrode (BE) and splits to the right (between the BE and the DR) and to the left (between the ME and the DR). It should be noted that most of the ink (about 67%) flows to the left. An electric potential difference between the electrodes and the DR generates an electric field, which

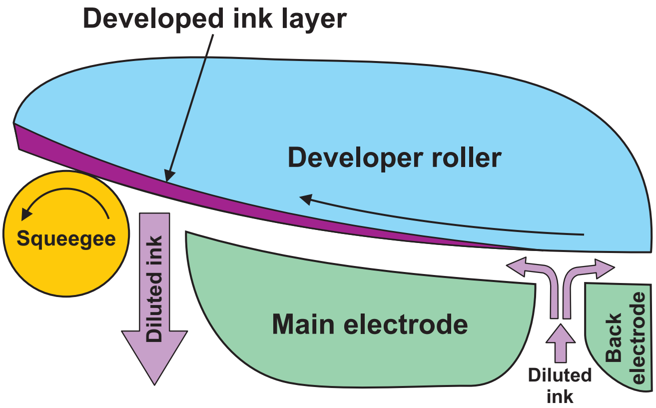

FIG. 2. Schematic representation of the gap between the main electrode and developer roller in which the ink flows. Reprinted with permission of IS&T: The Society for Imaging Science and Technology sole copyright owners of the NIP24: International Conference on Digital Printing Technologies and Digital Fabrication 2008 [41].

results in electric forces acting on the charged ink particles. The direction of the electric-field vector is radially outwards from the DR. Because of the negative charge on the ink particles, the electric force attracts the ink particles toward the DR surface. The narrow gap between the ME and the DR (350 μm) and the high applied voltage (1500 V) result in a very strong electric field (on the order of 10^3 V/mm), leading to the onset of highly chaotic electroconvective ionic transport, with subsequent chaotic mixing [29] of the charged species.

We now stress a few additional considerations before proceeding to the ultimate choice of physical model that would allow the deepest insight into the physics governing the electro-osmotic flow in the gap between the ME and the DR. First, due to the narrow gap between the ME and the DR (350 μm), the electric-field vector and the fluid-velocity vector are almost perpendicular to each other—the electric field is radial, while the flow velocity is tangential. Second, the arc length along which the ink flow develops is more than fifty times longer than the ME-DR gap, which enables us to neglect the curvature and to work within a rectangular domain. Third, due to the shear flow induced by the rotating DR, it is to be expected that in the plane of the DR motion the ECI suppressed (at least in the vicinity of the DR) [42], contributing to high printing quality. However, in reality, the width of the ME-DR gap is about 80 cm, which means that the flow is fully 3D and is thus much more complicated. In fact, close to the DR surface the ECI is indeed suppressed in the plane of the DR motion. However, as the rotating DR does not impose spanwise velocity, the ECI can develop unhindered in the spanwise direction and be further advected downstream. The ECI footprints developed in the vicinity of the top upper DR boundary can cause nonuniform concentrations of ink (streaks) on the DR surface and thereby significantly impair the printing quality. Fourth, the IsoparTM-L, comprising a nonsymmetric nonbinary electrolyte (see Fig. 1), is modeled as an electrolyte consisting of a single positively charged species and two negatively charged species. The charge valence of the positively charged species and one of the negatively charged species is ± unity, while the charge valence of the polymeric ink species is $O(10^3)$. The three species are diluted within a nonpolar solvent (i.e., mineral oil) and are subjected to a strong electric field (order of 10^3 V/mm) during the printing process. Lastly, an additional challenge typical of this kind of electro-osmotic flow is to accurately resolve the EDL, whose thickness can be of the order of hundreds of nanometers [43].

All the above considerations lead us to restrict our analysis of the ECI characteristics typical of the ME-DR gap to 2D electro-osmotic flow in the plane perpendicular to the plane of the DR motion. As mentioned above, in this plane, the ECI development is not affected by the DR motion, so both horizontal boundaries of the 2D domain can be assumed to be stationary. Note also that in

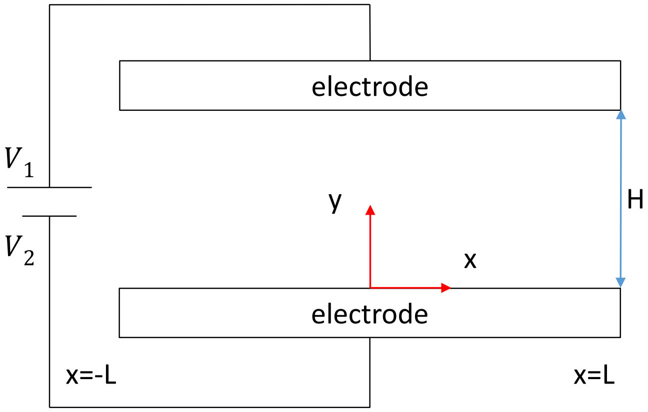

FIG. 3. Schematics of the geometry.

the framework of the current study we focus only on the small internal segment of the ME-DR gap, which allows us to impose periodic boundary conditions in the spanwise direction. Finally, even though the DR is, in reality, polymer coated, we model it as an open electrode to avoid the need to explicitly address the "crowding" effect that occurs on blocking electrodes in highly concentrated electrolytes [44]. It is believed that a fundamental investigation of the ECI characteristics typical of this configuration, albeit simplified compared with the full thee-dimensional (3D) setup, is important for further improving the printing quality. While the motivation for the analysis of this particular setup lies primarily in applications relevant to digital printing technologies, the setup under consideration can also be found in scenarios relating to the separation of organic pollutants and to surface coating technologies. To the best of our knowledge, this study is the first of its kind for the above-mentioned setup, in which the spatiotemporal characteristics of the ECI are elucidated by means of an extensive parametric study and by characterizing the differences between the ECI in that setup and its counterpart typical of a symmetric binary electrolyte.

II. PHYSICAL MODEL

A. Geometry and governing equations

We consider the electroconvective flow developing in a rectangular 2D domain of dimensions $\pm L \times H$, which is typical of the configuration presented in Fig. 3. The configuration is confined by two open electrodes, one at the top and the other at the bottom, held at constant V_1 and V_2 electric potentials, respectively (Fig. 3). The 2D domain is assumed to be periodic in the horizontal direction.

We now introduce the following scales characterizing the electroconvective flow typical of the above configuration:

$$t_{\text{diff}} = \frac{H^2}{D^+}, \quad V_T = \frac{RT}{z^+F}, \quad u_0 = \frac{\varepsilon}{\eta H} V_T^2, \quad p_0 = \frac{\eta u_0}{H}, \quad J_0 = \frac{D^+ c_0^+}{H}, \quad I_0 = \frac{F z^+ D^+ c_0^+}{H}, \quad (1)$$

where t_{diff} is the diffusion time, V_T is the thermal voltage, c_0 is the initial molar concentration of the bulk, u_0, p_0, J_0, and I_0 are the characteristic velocity, pressure, ionic flux, and current density, respectively, and the superscript $^+$ refers to the physical property taken for the positively charged species (cation). The full set of nondimensional equations governing the electroconvective flow of the nonsymmetric electrolyte consisting of n charged species is

$$\nabla \cdot \boldsymbol{u} = 0, \tag{2}$$

$$\frac{1}{Sc}\left(\frac{\partial \boldsymbol{u}}{\partial t} + Pe\boldsymbol{u} \cdot \nabla \boldsymbol{u}\right) = -\nabla p + \nabla^2 \boldsymbol{u} - \frac{1}{2\epsilon^2}\left(\sum_{i=1}^{n} z_{r_i} c_i\right)\nabla \psi, \tag{3}$$

$$-2\epsilon^2 \nabla^2 \psi = \sum_{i=1}^{n} z_{r_i} c_i, \tag{4}$$

$$\frac{\partial c_i}{\partial t} = -\nabla \cdot \boldsymbol{J}_i, \tag{5}$$

$$\boldsymbol{J}_i = Pec_i\boldsymbol{u} - D_{r_i}\nabla c_i - D_{r_i} z_{r_i} c_i \nabla \psi, \tag{6}$$

where the time, length, velocity, concentration, pressure, electric potential, ionic flux, and current density fields are normalized as

$$t = \frac{\tilde{t}}{t_{\text{diff}}}, \quad \boldsymbol{x} = \frac{\tilde{\boldsymbol{x}}}{H}, \quad \boldsymbol{u} = \frac{\tilde{\boldsymbol{u}}}{u_0}, \quad c_i = \frac{\tilde{c}_i}{c_0^+}, \quad p = \frac{\tilde{p}}{p_0}, \quad \psi = \frac{\tilde{\psi}}{V_T}, \quad \boldsymbol{J}_i = \frac{\tilde{\boldsymbol{J}}_i}{J_0}, \quad I_y = \frac{\tilde{I}_y}{I_0}, \tag{7}$$

where $\boldsymbol{x}$ corresponds to the spatial coordinate, $Sc = \eta/\rho D^+$ is the Schmidt number, $Pe = u_0 H/D^+$ is the Péclet number, and $\epsilon = \lambda_D/H$ is the nondimensional electrostatic screening length. The species are denoted by the subscripts $i = 1, 2, 3$, corresponding to the cation species of charge valence z^+, the anion species of charge valence z^-, and the third negatively charged species of charge valence Mz^-, respectively. Here $\lambda_D = [\varepsilon RT/2(z^+F)^2 c_0^+]^{1/2}$ is the Debye length, and the nondimensional parameters $z_{r_i} = z_i/z^+$ and $D_{r_i} = D_i/D^+$, correspond to the charge valence ratio and the molecular diffusivity ratio, respectively. The nondimensional surface-averaged electric current density is calculated by

$$I_y = -\frac{1}{AR}\int_{x=-AR/2}^{AR/2} \left[\sum_{i=1}^{n} z_{r_i} J_{i_y} - 2\epsilon^2 \frac{\partial^2 \psi}{\partial y \partial t}\right]\Bigg|_{x,\, y=y_0,\, t} dx, \tag{8}$$

where $AR = 2L/H$ is the aspect ratio of the rectangular computational domain. The first term in the above expression corresponds to the charged species passing through the given plane, while the second term, corresponding to the displacement current density, accounts for the time-varying electric field. Note that Eqs. (2)–(6) and (8) formulated for a general nonsymmetric electrolyte consisting of n charged species are straightforwardly reduced to the system governing the EC of a symmetric binary electrolyte by setting $n = 2$, $z_{r_1} = -z_{r_2} = 1$, and $D_{r_1} = D_{r_2} = 1$.

B. Representative property values

Recalling that the current research aims at addressing ECI typical of digital printing setups, it is appropriate to shortly survey here representative property values and basic assumptions typical of the digital printing process under consideration. This will further allow us to determine the range of operating conditions in terms of nondimensional groups described in the previous section. A list of the physical properties of the electrolyte (consisting of charge director and ink) and geometric characteristics of the setup under considerations are given in Table I.

It is assumed that the electric dissociation of the initially electrically neutral electrolyte into cations, anions, and ink species takes place immediately after exposing the electrolyte to the electric field. All through the simulation the ink is treated as a third species of constant charge valence, so that no electrochemical reactions and no recombination dynamics of the electric charge are taken into account. The operation characteristics H and T, as well as the specific values of electrolyte properties ρ, η, and ε_0 listed in Table I were obtained through internal communication with HP Indigo. These properties are assumed to be constant with no dependence on instantaneous local variations of all three species. See the Supplemental Material [45] for the way of calculating

TABLE I. Representative property and geometry values.

Description	Designation	Value	Units
Distance between electrodes	H	350	μm
Mixture density	ρ	765	kg m^{-3}
Mixture dynamic viscosity	η	9.615×10^{-4}	Pa s
Mixture temperature	T	30	°C
Mixture permittivity	ε	1.77×10^{-11}	F m^{-1}
Molecular diffusivity of cation species	D_1	1.25687×10^{-10}	m^2 s^{-1}
Molecular diffusivity of anion species	D_2	1.25687×10^{-10}	m^2 s^{-1}
Molecular diffusivity of ink species	D_3	2.51373×10^{-13}	m^2 s^{-1}
Initial bulk concentration of cation species	c_0^+	6.4301×10^{-5}	mol m^{-3}
Initial bulk concentration of anion species	c_0^-	4.6951×10^{-5}	mol m^{-3}
Initial bulk concentration of ink species	c_0^{ink}	4.6951×10^{-9}	mol m^{-3}
Charge valence of cation species	z_1	1	–
Charge valence of anion species	z_2	-1	–
Charge valence of ink species	z_3	-3695	–

the values of molecular diffusivity D, charge valence z, and initial bulk concentration c_0 of the electrolyte species given in Table I.

Based on the values of the physical properties given in Table I, the values of characteristic nondimensional groups typical of the considered configuration can be obtained as given in Table II. The quantity M corresponds to the ink to anion charge valence ratio, whereas c_r corresponds to the initial ratio of the ink concentration to anion species within the electrically neutral bulk. Note that the physical properties appearing in Table I yield the values of $\epsilon = 5.52 \times 10^{-4}$ and $c_r = 10^{-4}$. Both values are critical when investigating the characteristics of instability onset of the considered electroconvective flow. For this reason, the simulations were performed for the range of $\epsilon \in [2.5 \times 10^{-4}, 10^{-3}]$ and $c_r \in [2 \times 10^{-5}, 5 \times 10^{-4}]$. It should be also noted that the currently used value of the nondimensional thermal voltage equal to $V = 4 \times 10^4$ corresponds to values of the electric field of $O(10^3)$ V/mm typical of digital printing setups.

TABLE II. Representative values of nondimensional groups.

Description	Designation	Value
Schmidt number	Sc	10^4
Péclet number	Pe	0.1
Voltage	V	4×10^4
Electrostatic screening length	ϵ	$[2.5 \times 10^{-4}, 10^{-3}]$
Initial concentration ratio	c_r	$[2 \times 10^{-5}, 5 \times 10^{-4}]$
Charge valence ratio of cation species	z_{r_1}	1
Charge valence ratio of anion species	z_{r_2}	-1
Charge valence index of ink species	M	3695
Molecular diffusivity ratio of cation species	D_{r_1}	1
Molecular diffusivity ratio of anion species	D_{r_2}	1
Molecular diffusivity ratio of ink species	D_{r_3}	0.002
Aspect ratio	AR	6

C. Boundary, operating, and initial conditions

The schematics of the two-electrode configuration operating with a nonsymmetric electrolyte consisting of three charged species of charge valences z^+, z^-, and Mz^- is shown in Fig. 3. The boundary conditions (BCs) for the concentration fields are as follows: the bottom electrode is completely permeable to cations and impermeable to the two negatively charged species and the top electrode is impermeable to cations and is completely permeable to the two negatively charged species. The bottom and top electrodes are held at constant electric potentials equal to $V_2 = -V/2$ and $V_1 = V/2$, respectively. Nonslip BCs for all the velocity components are set on the surfaces of the two electrodes. Periodic BCs for all the fields are set in the x direction. The applied BCs in a nondimensional formulation are given by

$$\begin{aligned} y = 0: &\quad \frac{\partial c_1}{\partial y} = 0, \quad J_{y_2} = J_{y_3} = 0, \quad \psi = -\frac{V}{2}, \quad \boldsymbol{u} = 0, \\ y = 1: &\quad J_{y_1} = 0, \quad \frac{\partial c_2}{\partial y} = \frac{\partial c_3}{\partial y} = 0, \quad \psi = \frac{V}{2}, \quad \boldsymbol{u} = 0, \end{aligned} \tag{9}$$

so that the electric field goes from the upper to the bottom electrode. We note, in passing, that the above BCs can be straightforwardly adapted for the case of a symmetric binary electrolyte by simply omitting the relationships with index $i = 3$.

The initial conditions (ICs) for the concentration fields have to provide electroneutrality of the diffusion layer (DL) of the electrolyte, which, for the case of the nonsymmetric electrolyte consisting of three charged species, gives

$$c_1 + z_{r_2} c_2 + M z_{r_2} c_r c_2 = 0, \tag{10}$$

where $c_r = c_3/c_2$ at $t = 0$. Note that the above relationship can be straightforwardly adapted to the symmetric binary electrolyte by simply assigning the values $z_{r_2} = -1$ and $c_r = 0$. Zero initial values are set for the electric potential and velocity vector fields within the computational domain.

III. NUMERICAL METHOD

The electrically driven flow (EDF) typical of the two-electrode configuration under consideration was simulated by utilizing the open-source package RHEOTOOL [46]. The package facilitates the simulation of a wide spectrum of non-Newtonian flows and EDFs. In particular, the RHEOEFOAM solver, which is a part of RHEOTOOL, was used to solve the Poisson-Nernst-Planck (PNP) equations [Eqs. (4) and (5)], while the two-way coupling with the continuity [Eq. (2)] and Navier-Stokes [Eq. (3)] equations are a built-in feature of the RHEOTOOL implemented on top of OPENFOAM [47]. In accordance with the OPENFOAM formalism, the spatial discretization of all the differential operators was performed by utilizing the standard second-order finite-volume method [48], while the second-order backward difference was used for the time discretization. All the simulations were performed on a standard Unix server equipped with two Intel Xeon 12C Processors (Model E5-2697v2, 24 cores in total) and 128 GB RAM. The solver has previously been extensively verified for simulation of the flow typical of induced-charge electro-osmosis (ICEO) around a conducting cylinder and of EC typical of an ion-selective membrane [46]. See the Supplemental Material [45] for an extensive verification and grid independence study for the configurations relevant to the current research.

IV. RESULTS AND DISCUSSION

In keeping with the boundary and operating conditions utilized in the framework of the present study, it is clear that the electroconvective flow under consideration operates in an overlimiting regime, exhibiting the development of electro-osmotic flow of the second kind [49–52] driving the ECI phenomenon. We recall that the considered nonsymmetric electrolyte consists of the three species. One of these species comprises large micron-sized polymer particles, each of which is encircled by thousands of anions and is thus characterized by a significantly higher [by an order of $O(10^3)$] charge valence and by significantly lower [also by an order of $O(10^3)$] diffusivity values compared with two other species (anions and cations). Both anions and cations, which will have instantly dissociated from the charge director under the action of the strong electric field, have the same diffusivity and charge valence (± unity) values.

A. Pre-electroconvective-instability ionic transport

We start by investigating the ionic transport typical of the considered configuration in a very short time interval of the order of $O(\epsilon^2)$, starting immediately after the electric field is imposed and ending with the ECI onset. Within this time interval, no electroconvection takes place and the ionic transport can be accurately predicted simply by solution of the one-dimensional (1D) PNP equations (4) and (5). The equations were solved by an in-house-developed MATLAB script. See the Supplemental Material [45] for extensive verification of the in-house-developed MATLAB script.

The results presented below shed light on the fundamental differences between the ionic dynamics typical of an electrolytic cell operating at high voltages within a symmetric binary electrolyte and the ionic dynamics within a nonsymmetric electrolyte composed of three species. Figure 4(a) compares the instantaneous distribution of the space-charge density ρ_E of the two electrolytes obtained for the values of $\epsilon = 2.5 \times 10^{-4}$ and $c_r = 10^{-4}$. The specific value of the time instance was chosen because it exposes the phenomenon of separation between the ink and the anion species, as discussed below. Nonzero values of the space-charge density indicate the width of the ESC region at a given time instance. In both cases shown in Fig. 4(a), the ionic transport within the electrolyte between the two open electrodes is characterized by the presence of two ESC regions, each starting to develop at one of the electrodes and progressing inwards with time. According to the schematics of the configuration under consideration (Fig. 3), the externally imposed electric field is directed from the right electrode toward the left electrode; thus, the left and the right spikes separate the neutral bulk from the positively and negatively charged ESC regions, respectively. As expected, the ESC width of the symmetric binary electrolyte preserves its symmetry over time relative to the center of the electrolytic cell. For the nonsymmetric electrolyte, the picture is quite different and is characterized by two unique features. First, there is an additional third ESC region, characterized by a smaller spike and clearly indicating the separation of the two negatively charged species. Second, each ESC region is characterized by a different propagation rate.

To gain additional insight into the spatiotemporal charge distribution within the nonsymmetric electrolyte, we decomposed the space-charge density ρ_E into the terms contributed by each species, namely, z_1c_1, z_2c_2, and $z_3c_3 = Mz_2c_3$.[1] The spatial distribution of the absolute value of each term contributing to ρ_E taken at $t = 1.7 \times 10^{-6}$ is presented in Fig. 4(b). The spatial distribution shown in Fig. 4(b) can be semantically split into four zones. Zones 1 and 4 represent the positively and the negatively charged ESCs, respectively. Zone 3 corresponds to the electrically neutral bulk whose composition is the same as that determined by the ICs [Eq. (10)]. Generally speaking, zone 3 is not unique for a nonsymmetric electrolyte: electrically neutral bulk is common in the ionic transport of the symmetric binary electrolyte (see, e.g., Refs. [28,53]). In contrast, zone 2 is an exclusive feature typical of a nonsymmetric electrolyte in which one of the species has much higher electro-osmotic mobility, giving rise to a separation phenomenon between the two negatively charged species. Specifically, in the current study, the $D_{r_i}z_{r_i}$ multiplier entering the ionic flux [Eq. (6)] and representing the electro-osmotic mobility of the ith species is more than seven times higher for the $i = 3$ species than for the $i = 2$ species. For this reason, zones 1 and 2 are entirely depleted of the $i = 3$ species, as its propagation rate is much higher than that of the $i = 2$

---

[1] Note that this decomposition has been already introduced in Eq. (10) as the IC providing electroneutrality of the nonsymmetric electrolyte.

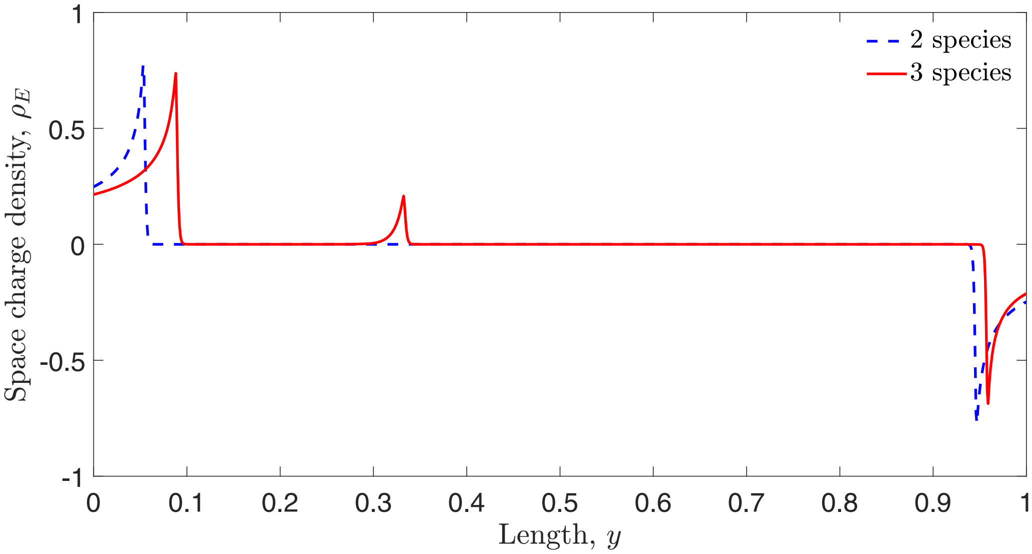

(a)

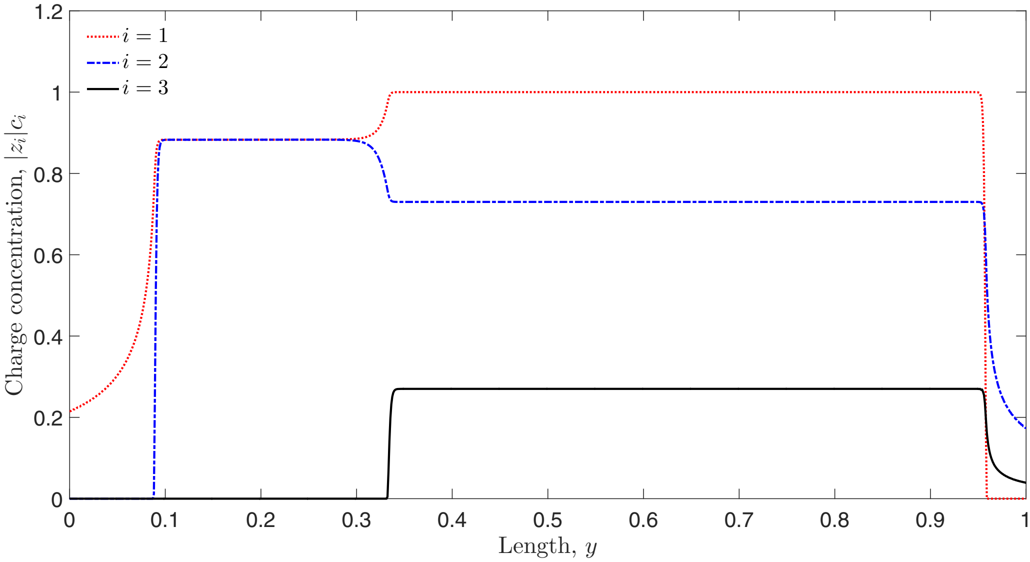

(b)

FIG. 4. 1D ionic transport within an electrolyte between two open electrodes. The results were obtained for the values of $\epsilon = 2.5 \times 10^{-4}$, $t = 1.7 \times 10^{-6}$, and for three species $c_r = 10^{-4}$: (a) distribution of the space-charge density ρ_E; (b) spatial distribution of the terms $|z_i|c_i$ ($i = 1$ for cations, 2 for anions, and 3 for the third species) contributing to the space-charge density ρ_E.

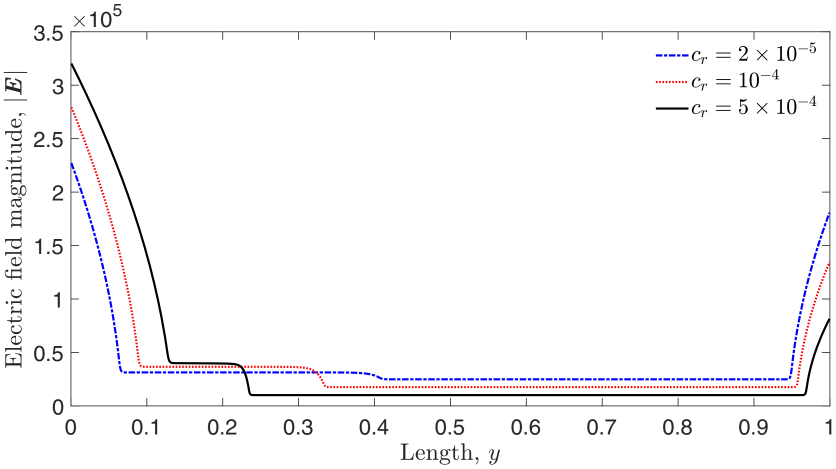

FIG. 5. Spatial distribution of the electric-field magnitude $|\boldsymbol{E}|$ for different c_r values. The results were obtained for the values of $\epsilon = 2.5 \times 10^{-4}$ and $t = 1.7 \times 10^{-6}$.

species. Remarkably, the $i = 1$ and $i = 2$ species adjust themselves differently in zone 2 compared with zone 3 in order to preserve electroneutrality in the region entirely depleted of the $i = 3$ species.[2]

The nonequal propagation rates of the $i = 1$ and $i = 2$ species, when moving away from the right and left electrodes, respectively, toward the center of the electrolytic cell can be explained in terms of the spatial distribution of the electric field magnitude $|\boldsymbol{E}|$ shown in Fig. 5.

We first focus on the distribution of the electric-field magnitude in the ESC region adjacent to the right electrode. Close to the right electrode, there is no separation between the two negatively charged species [Fig. 4(b)]; thus, each species contributes to the ionic flux in this region proportionally to its concentration multiplied by the corresponding charge valence. As a result, this region is dominated by the negative charges that screen the imposed electric potential, as reflected by the rapid decrease of the electric field until it reaches a minimum constant value characterizing the bulk region and eventually governing the propagation rate of the cations away from the right electrode. The mechanism driving the negatively charged species away from the left electrode is different. As already mentioned, there is a separation between the species [Fig. 4(b)] in this region due to their different electro-osmotic mobilities, and the negatively charged $i = 3$ species outstrips the $i = 2$ species on its way toward the right electrode. Zone 2 is thus entirely depleted of the $i = 3$ species, which leads to a decrease in the concentration of the $i = 1$ species [Fig. 4(b)] so as to preserve the electroneutrality of the electrolyte in this region. As a result, the screening of the imposed electric potential due to the presence of the $i = 1$ species is lower than that in the ESC region adjacent to the right electrode.[3] This finding is reflected by the higher value of the electric-field magnitude $|\boldsymbol{E}|$ prevailing in zone 2 compared with that prevailing in zone 3 (Fig. 5), which determines the higher propagation rate of the anion species ($i = 2$) toward the center of the electrolytic cell compared with that of the cation species ($i = 1$).

---

[2] The electroneutrality is preserved over the whole width of zone 2, except for the rear front of the $i = 3$ species, consistently with the spike of ρ_E observed at $y \approx 0.33$, as shown in Fig. 4(a).

[3] Recall that in the ESC region adjacent to the right electrode, the screening effect of the imposed electric potential is due to the presence of the two negatively charged species $i = 2$ and $i = 3$.

B. Nonsymmetric onset of the electroconvective instability

The symmetry-breaking phenomenon observed for ionic transport within a nonbinary 1D electrolyte is also manifested in the onset and development of ECI in its 2D counterpart. To cover the wide spectrum of representative ECI scenarios, the simulations were performed for the set of $\epsilon = [2.5 \times 10^{-4}; 5 \times 10^{-4}; 10^{-3}]$ and $c_r = [2 \times 10^{-5}; 10^{-4}; 5 \times 10^{-4}]$ values. Following the known mechanism described in Refs. [49–52], the electro-osmotic flow of the second kind starts within the electrolytic cell operating in the overlimiting regime with an external vertically applied electric field and drives the ECI phenomenon. The instability is initiated as a result of disturbances in the electric field introduced in the tangential[4] direction. In real experiments, the disturbance is typically attributed to imperfections intrinsic in the experimental setup, while in numerical simulations the instability is induced by rounding and truncation errors as a result of limited machine precision and discretization errors, respectively. The ECI is manifested in the creation of a series of vortex pairs (VPs) occupying the whole ESC and accelerating the contraction of the double-layer region. Note also that in contrast to the membrane-bulk configuration, in the current electrolytic cell confined by two electrodes the EDL is attached to the moving ESC front, while the development of VPs takes place at the DL-ESC interface. Note that for finite (no matter how small) values of the Debye length, the VPs do not form immediately after applying the external voltage; rather, they can be recognized clearly only after the ESC reaches a critical width, or alternatively, after a certain critical time value, both depending on the Debye length and the external voltage. Figure 6 presents two typical scenarios for the ECI onset as a function of ϵ and c_r values. See the Supplemental Material [45] for the entire spreadsheet encompassing the whole set of ϵ and c_r values.

To facilitate an understanding of the mechanism of the ECI onset, the 2D concentration distributions for the $i = 1$ and $i = 2$ species are presented together with the corresponding 1D counterparts, as there is a strong resemblance between the ionic transport within both types of electrolytic cell prior to and at the very beginning of the ECI onset. Note also that only half of the domain is shown for the 2D concentration distribution, as presenting the whole domain does not provide any additional information. As an outcome of the significant difference between the electro-osmotic mobilities of $i = 3$ and the two other species, the ECI onset does not take place simultaneously on the ESC-DL interfaces adjacent to the two electrodes, as reflected by the t_1 and t_2 values corresponding to the instances at which the appearance of VPs is first observed in the vicinity of the bottom and top electrodes, respectively. In fact, for the two specific configurations shown in Fig. 6, time t_2 is longer than time t_1 by about a factor of two. The observed differences in t_1 and t_2 are consistent with the corresponding concentration distributions reflecting the ionic transport within the 1D electrolytic cell. It is evident that as a consequence of different propagation rates of the species determined by their electro-osmotic mobilities and the electric-field distribution (see also Fig. 5) the width of the ESC layer adjacent to the left cathode is larger than that adjacent to the right anode. Consequently, the ESC layer adjacent to the cathode reaches the critical width before its counterpart adjacent to the anode, which promotes earlier formation of the ECI VPs within the cathode ESC. In summary, a small amount of a charged species of significantly higher (more than seven times in the current study) electro-osmotic mobility as an electrolyte additive delays the ECI onset in the vicinity of oppositely charged electrode, which constitutes a convenient way for controlling the onset of the ECI in the 2D electrolytic cell.

To quantify the nonsymmetric ECI onset, we introduce the relative time difference τ between t_2 and t_1, determined as

$$\tau = \frac{t_2 - t_1}{t_2} \times 100\%, \tag{11}$$

and summarize the dependance of τ on the entire set of c_r and ϵ values in Table III.

---

[4] That is, in the direction perpendicular to the externally applied electric field.

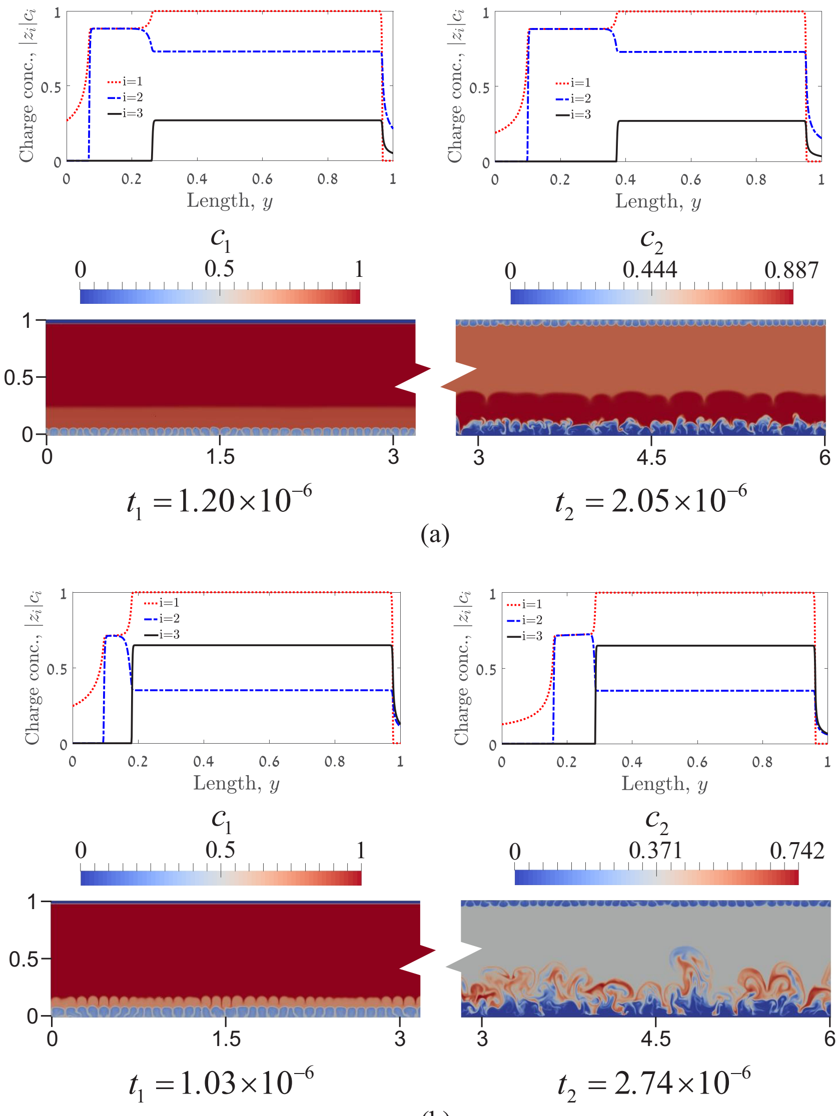

(a)

(b)

FIG. 6. ECI patterns of cation and anion species a short time after its generation, including 1D charge concentration curves for each species. (a) $\epsilon = 2.5 \times 10^{-4}$, $c_r = 10^{-4}$. (b) $\epsilon = 2.5 \times 10^{-4}$, $c_r = 5 \times 10^{-4}$.

TABLE III. Values of the relative time difference τ (in percent) between the times characterizing the onset of the ECI at the cathode and at the anode ESCs.

	ϵ		
c_r	2.5×10^{-4}	5×10^{-4}	10^{-3}
2×10^{-5}	19.88	18.61	9.37
10^{-4}	41.46	41.24	25.52
5×10^{-4}	62.41	60.86	23.84

TABLE IV. Nondimensional wave numbers k_1 and k_2 in the vicinity of the cathode and anode, respectively.

	ϵ			
c_r	2.5×10^{-4}	5×10^{-4}	10^{-3}	
2×10^{-5}	k_1	102	46	22
	k_2	98	47	19
10^{-4}	k_1	88	39	19
	k_2	95	40	20
5×10^{-4}	k_1	71	30	15
	k_2	83	39	16

It can be seen that the relative time difference τ increases with c_r. The increase is more pronounced for lower values of ϵ corresponding to the overall higher concentrations of charged species. As expected, the lowest τ was obtained for the highest value of ϵ and the lowest value of c_r, corresponding to the lowest values of both the concentrations of the charged species and specifically the lowest concentration of the $i = 3$ species.

The generation of secondary VP series in zone 2 by means of the c_1 patterns is an additional characteristic property of the ECI of a nonsymmetric electrolyte typical of high c_r values. The appearance of a secondary VP series located in zone 2, as early as t_1 time, can be clearly recognized close to the primary VP series located in zone 1 next to the cathode, as shown in Fig. 6(b). It is clear that the very appearance of the secondary VP series is closely related to the c_r value determining the magnitude of the space-charge density in the vicinity of interface between zones 2 and 3, although precise determination of the critical c_r value responsible for the generation of secondary VP series is beyond the scope of the current study.

We now introduce the nondimensional wave number k as an additional metric quantifying the characteristics of the onset of the ECI in the 2D electrolytic cell. The wave number is defined as the instantaneous number of VPs located along a length $2L$ in the x direction (see Fig. 3):

$$k = \frac{2\pi N_{VP}}{AR}. \tag{12}$$

In keeping with Refs. [54–56], the wave number k is obtained on the basis of the 2D contours of the cation and anion concentrations, where k_1 and k_2 for the cation and the anion species, respectively, are calculated in the vicinity of the bottom (cathode) and the top (anode) electrodes. The values of k_1 and k_2 obtained for the whole range of c_r and ϵ values are given in Table IV.

The wave-number–time relationship can be modeled by the power law, as follows from Fig. 7 presenting the least-squares best fit for the wave-number–time dependance for the cathode and the anode. Note that the value of the VP wave number on the anode is consistently higher than that on the cathode. The symmetry-breaking character of the observed ECI is clearly evinced by different power and coefficient values governing the power law for the cathode and the anode. The differences in the power values are not particularly marked, indicating that at the very beginning of ECI the diffusive VPs growth at both electrodes is governed by approximately $1/\sqrt{t}$ time scaling, as was also reported in Ref. [54]. At the same time, a greater than twofold difference is observed for the coefficient values governing the anode and cathode wave-number–time relationships, which can be explained by the effectively different diffusivity values of the electrolyte in these regions at the ECI onset. In fact, at the ECI onset the electrolyte consists of only $i = 1$ species in the vicinity of the cathode, while in the vicinity of the anode it consists of $i = 2$ and $i = 3$ species and is therefore characterized by an effectively lower diffusivity.

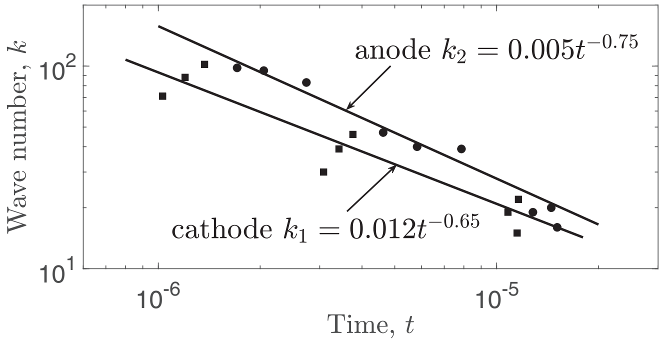

FIG. 7. The VP wave number versus time at the ECI onset for the anode (black circles) and the cathode (black squares) in the 2D electrolytic cell.

V. CONCLUSIONS

Ionic transport within 1D and 2D electrolytic cells confined by two open electrodes and operating at high voltage with an initially electrically neutral nonsymmetric electrolyte consisting of one positively charged species and two negatively charged species was investigated comprehensively. The major focus of the study was placed on elucidating the fundamental differences between the ionic transport typical of symmetric binary and nonsymmetric electrolytes within 1D and 2D electrolytic cells. The problem was analyzed by means of a parametric study aiming at revealing the impact of the values of the electrostatic screening length ϵ and the ratio between the initial concentrations of the two negatively charged species, c_r, on the ionic transport characteristics for the 1D configuration and on the onset of the ECI for the 2D configuration.

Specifically, for the 1D electrolytic cell, it was found that, similarly to its symmetric binary counterpart, the DL of a nonsymmetric electrolyte tends to preserve its electroneutrality throughout the whole ionic transport process. This basic characteristic property, coupled with significantly different electro-osmotic mobilities of the two negatively charged species, distinguishes the ionic transport within a nonsymmetric electrolyte from that typical of its symmetric binary counterpart in terms of features unique of the nonsymmetric electrolyte: the presence of three ESC regions, each corresponding to one of the species, the separation of the two negatively charged species, and finally the different propagation rates of each ESC region. The insights obtained from the analysis of the ionic transport within a 1D electrolytic cell were subsequently used to obtain a deeper understanding of the onset of the ECI for a 2D electrolytic cell operating with a nonsymmetric electrolyte. The nonsymmetric development of the ECI was explained and thoroughly investigated in terms of three major characteristics: the nonsymmetric vortical initial state, the nonsymmetric value of the wave number of the VPs, and finally, the double VP series adjacent to the cathode region observed at sufficiently high c_r values. All the observed characteristics were visualized by presenting the concentration fields of the cation and the anion species, each obtained at the corresponding ECI onset.

Although the current study is restricted to an analysis of 2D ionic transport within an electrolytic cell confined by two open electrodes (at the top and bottom) and periodic BCs in the horizontal direction, it constitutes an important milestone toward determining the main characteristics of ECI typical of a nonsymmetric electrolyte at high voltage. By further applying the modified PNP equations presented in Refs. [44,57–60], the study can be extended straightforwardly to the simulation of ionic transport within electrolytic cells confined by blocking electrodes, which is the focus of our ongoing research. This ongoing research is designed to investigate the accumulation of charged species in the vicinity of the two electrodes and their impact on the ECI onset—a mechanism of significant importance in the surface coating and digital printing industries. An additional promising research direction is applying a modulated electric field to a nonsymmetric electrolyte for producing miniaturized electric pumps and microfluidic separators relevant to the enhanced cooling of electronic components and liquid-purification applications.

ACKNOWLEDGMENTS

The study was supported by Hewlett Packard Indigo Division Ltd. We would like to express our thanks to Y. Green for fruitful discussions during the preparation of this paper.

[1] L.-J. Cheng and L. J. Guo, Rectified ion transport through concentration gradient in homogeneous silica nanochannels, Nano Lett. **7**, 3165 (2007).

[2] Z. Zhang, S. Yang, P. Zhang, J. Zhang, G. Chen, and X. Feng, Mechanically strong mxene/kevlar nanofiber composite membranes as high-performance nanofluidic osmotic power generators, Nat. Commun. **10**, 1 (2019).

[3] Y. Green, Y. Edri, and G. Yossifon, Asymmetry-induced electric current rectification in permselective systems, Phys. Rev. E **92**, 033018 (2015).

[4] D. Brogioli, Extracting Renewable Energy from a Salinity Difference Using a Capacitor, Phys. Rev. Lett. **103**, 058501 (2009).

[5] F. La Mantia, M. Pasta, H. D. Deshazer, B. E. Logan, and Y. Cui, Batteries for efficient energy extraction from a water salinity difference, Nano Lett. **11**, 1810 (2011).

[6] F. H. van der Heyden, D. J. Bonthuis, D. Stein, C. Meyer, and C. Dekker, Power generation by pressure-driven transport of ions in nanofluidic channels, Nano Lett. **7**, 1022 (2007).

[7] M. D. Tikekar, S. Choudhury, Z. Tu, and L. A. Archer, Design principles for electrolytes and interfaces for stable lithium-metal batteries, Nat. Energy **1**, 1 (2016).

[8] G. Li, L. A. Archer, and D. L. Koch, Electroconvection in a Viscoelastic Electrolyte, Phys. Rev. Lett. **122**, 124501 (2019).

[9] H. Chang and L. Yeo, *Electrokinetically Driven Microfluidics and Nanofluidics* (Cambridge University Press, New York, 2010).

[10] S. A. M. Shaegh, N.-T. Nguyen, and S. H. Chan, A review on membraneless laminar flow-based fuel cells, Int. J. Hydrogen Energy **36**, 5675 (2011).

[11] N. A. Mishchuk, T. Heldal, T. Volden, J. Auerswald, and H. Knapp, Micropump based on electroosmosis of the second kind, Electrophoresis **30**, 3499 (2009).

[12] S. J. Kim, Y.-C. Wang, J. H. Lee, H. Jang, and J. Han, Concentration Polarization and Nonlinear Electrokinetic Flow Near a Nanofluidic Channel, Phys. Rev. Lett. **99**, 044501 (2007).

[13] S. M. Davidson, M. B. Andersen, and A. Mani, Chaotic Induced-Charge Electro-Osmosis, Phys. Rev. Lett. **112**, 128302 (2014).

[14] G. Jaffe, Theory of conductivity of semiconductors, Phys. Rev. **85**, 354 (1952).

[15] J. R. Macdonald, Theory of ac space-charge polarization effects in photoconductors, semiconductors, and electrolytes, Phys. Rev. **92**, 4 (1953).

[16] A. Meller, L. Nivon, and D. Branton, Voltage-Driven DNA Translocations through a Nanopore, Phys. Rev. Lett. **86**, 3435 (2001).

[17] A. Meller, A new tool for cell signalling research, Nat. Nanotechnol. **14**, 732 (2019).

[18] Y. Green, Current-voltage response for unipolar funnel-shaped nanochannel diodes, Phys. Rev. E **98**, 033114 (2018).

[19] Z. S. Siwy and S. Howorka, Engineered voltage-responsive nanopores, Chem. Soc. Rev. **39**, 1115 (2010).

[20] R. Karnik, R. Fan, M. Yue, D. Li, P. Yang, and A. Majumdar, Electrostatic control of ions and molecules in nanofluidic transistors, Nano Lett. **5**, 943 (2005).

[21] R. Karnik, C. Duan, K. Castelino, H. Daiguji, and A. Majumdar, Rectification of ionic current in a nanofluidic diode, Nano Lett. **7**, 547 (2007).

[22] W. Guan, R. Fan, and M. A. Reed, Field-effect reconfigurable nanofluidic ionic diodes, Nat. Commun. **2**, 1 (2011).

[23] R. Yan, W. Liang, R. Fan, and P. Yang, Nanofluidic diodes based on nanotube heterojunctions, Nano Lett. **9**, 3820 (2009).

[24] Y.-M. Lee, S.-J. Lee, C.-Y. Lee, and D.-Y. Chang, The multiphysics analysis of the metallic bipolar plate by the electrochemical micro-machining fabrication process, J. Power Sources **193**, 227 (2009).

[25] V. V. Nikonenko, A. V. Kovalenko, M. K. Urtenov, N. D. Pismenskaya, J. Han, P. Sistat, and G. Pourcelly, Desalination at overlimiting currents: State-of-the-art and perspectives, Desalination **342**, 85 (2014).

[26] S. Abdu, M. Martí-Calatayud, J. Wong, M. García-Gabaldón, and M. Wessling, Layer-by-layer modification of cation exchange membranes controls ion selectivity and water splitting., ACS Appl. Mater. Interfaces **6**, 1843 (2014).

[27] M. B. Andersen, D. M. Rogers, J. Mai, B. Schudel, A. V. Hatch, S. B. Rempe, and A. Mani, Spatiotemporal pH dynamics in concentration polarization near ion-selective membranes, Langmuir **30**, 7902 (2014).

[28] C. Druzgalski, M. Andersen, and A. Mani, Direct numerical simulation of electroconvective instability and hydrodynamic chaos near an ion-selective surface, Phys. Fluids **25**, 110804 (2013).

[29] C. Druzgalski and A. Mani, Statistical analysis of electroconvection near an ion-selective membrane in the highly chaotic regime, Phys. Rev. Fluids **1**, 073601 (2016).

[30] I. Rubinstein and B. Zaltzman, Electro-osmotically induced convection at a permselective membrane, Phys. Rev. E **62**, 2238 (2000).

[31] I. Rubinstein and B. Zaltzman, Electro-osmotic slip of the second kind and instability in concentration polarization at electrodialysis membranes, Math. Models Methods Appl. Sci. **11**, 263 (2001).

[32] I. Rubinstein and B. Zaltzman, Wave number selection in a nonequilibrium electro-osmotic instability, Phys. Rev. E **68**, 032501 (2003).

[33] I. Rubinstein, B. Zaltzman, and I. Lerman, Electroconvective instability in concentration polarization and nonequilibrium electro-osmotic slip, Phys. Rev. E **72**, 011505 (2005).

[34] I. Rubinshtein, B. Zaltzman, J. Pretz, and C. Linder, Experimental verification of the electroosmotic mechanism of overlimiting conductance through a cation exchange electrodialysis membrane, Russ. J. Electrochem. **38**, 853 (2002).

[35] S. M. Rubinstein, G. Manukyan, A. Staicu, I. Rubinstein, B. Zaltzman, R. G. H. Lammertink, F. Mugele, and M. Wessling, Direct Observation of a Nonequilibrium Electro-Osmotic Instability, Phys. Rev. Lett. **101**, 236101 (2008).

[36] T. Pundik, I. Rubinstein, and B. Zaltzman, Bulk electroconvection in electrolyte, Phys. Rev. E **72**, 061502 (2005).

[37] B. Zaltzman and I. Rubinstein, Electro-osmotic slip and electroconvective instability, J. Fluid Mech. **579**, 173 (2007).

[38] I. Rubinstein and B. Zaltzman, Equilibrium electro-osmotic instability in concentration polarization at a perfectly charge-selective interface, Phys. Rev. Fluids **2**, 093702 (2017).

[39] E. A. Demekhin, S. Amiroudine, G. S. Ganchenko, and N. Y. Khasmatulina, Thermoelectroconvection near charge-selective surfaces, Phys. Rev. E **91**, 063006 (2015).

[40] P. Forgacs and A. Teishev, Electro-rheological model of HP indigo electroInk, J. Imaging Sci. Technol. **57**, 30403 (2013).

[41] B. Tagansky, in *24th International Conference on Digital Printing Technologies/Digital Fabrication 2008, Technical Program and Proceedings* (Ink development in HP Indigo digital, 2008), pp. 799–802.

[42] A. Kourmatzis and J. S. Shrimpton, Characteristics of electrohydrodynamic roll structures in laminar planar Couette flow, J. Phys. D: Appl. Phys. **49**, 045503 (2016).

[43] P. A. Vázquez, M. Talmor, Seyed-Yagoobi, P. J. Traoré, and M. Yazdani, In-depth description of electrohydrodynamic conduction pumping of dielectric liquids: Physical model and regime analysis, Phys. Fluids **31**, 113601 (2019).

[44] M. Z. Bazant, B. D. Storey, and A. A. Kornyshev, Double Layer in Ionic Liquids: Overscreening Versus Crowding, Phys. Rev. Lett. **106**, 046102 (2011).

[45] See Supplemental Material at http://link.aps.org/supplemental/10.1103/PhysRevFluids.6.113701 for details on verification study, calculation of species properties and the whole set of ECI patterns.

[46] F. Pimenta and M. A. Alves, Numerical simulation of electrically-driven flows using openfoam, arXiv:1802.02843.

[47] H. G. Weller, G. Tabor, H. Jasak, and C. Fureby, A tensorial approach to computational continuum mechanics using object-oriented techniques, Comput. Phys. **12**, 620 (1998).

[48] S. V. Patankar and D. B. Spalding, A calculation procedure for heat, mass and momentum in three-dimensional parabolic fows, Int. J. Heat Mass Transfer **15**, 1787 (1972).

[49] S. S. Dukhin and N. A. Mishchuk, Disappearance of Limiting Current Phenomenon in the Case of a Granule of an Ion Exchanger, Colloid J. USSR **51**, 570 (1989).

[50] S. S. Dukhin, N. A. Mishchuk, and P. V. Takhistov, Electroosmosis of the second kind and unrestricted current increase in the mixed monolayer of an ion-exchanger, Colloid J. USSR **51**, 540 (1989).

[51] S. S. Dukhin, Electrokinetic phenomena of the second kind and their applications, Adv. Colloid Interface Sci. **35**, 173 (1991).

[52] N. Mishchuk, P. Takhistov *et al.*, Electroosmosis of the second kind and current through curved interface, Colloids Surf., A **181**, 131 (2001).

[53] E. Yariv, Asymptotic current-voltage relations for currents exceeding the diffusion limit, Phys. Rev. E **80**, 051201 (2009).

[54] Y. Green and G. Yossifon, Dynamical trapping of colloids at the stagnation points of electro-osmotic vortices of the second kind, Phys. Rev. E **87**, 033005 (2013).

[55] V. Shelistov, N. Nikitin, V. Kiriy, and E. Demekhin, A Sequence of Electrokinetic-Instability Bifurcations Resulting in a Chaotic-Flow Regime, in *Doklady Physics* (Pleiades Publishing, 2014), Vol. 59, pp. 166–169.

[56] R. Abu-Rjal, N. Leibowitz, S. Park, B. Zaltzman, I. Rubinstein, and G. Yossifon, Signature of electroconvective instability in transient galvanostatic and potentiostatic modes in a microchannel-nanoslot device, Phys. Rev. Fluids **4**, 084203 (2019).

[57] I. Borukhov, D. Andelman, and H. Orland, Steric Effects in Electrolytes: A Modified Poisson-Boltzmann Equation, Phys. Rev. Lett. **79**, 435 (1997).

[58] M. S. Kilic, M. Z. Bazant, and A. Ajdari, Steric effects in the dynamics of electrolytes at large applied voltages. II. modified Poisson-Nernst-Planck equations, Phys. Rev. E **75**, 021503 (2007).

[59] A. Yochelis, Spatial structure of electrical diffuse layers in highly concentrated electrolytes: A modified Poisson–Nernst–Planck approach, J. Phys. Chem. C **118**, 5716 (2014).

[60] N. Gavish, D. Elad, and A. Yochelis, From solvent-free to dilute electrolytes: Essential components for a continuum theory, J. Phys. Chem. Lett. **9**, 36 (2018).